Published in final edited form as:
Magn Reson Med. 2014 June ; 71(6): 2186–2196. doi:10.1002/mrm.24851.

Assessing Intrarenal Non-perfusion and Vascular Leakage in Acute Kidney Injury withzz ^{19}F MRI and Perfluorocarbon Nanoparticles

Lingzhi Hu[1], **Junjie Chen**[2], **Xiaoxia Yang**[2], **Angana Senpan**[2], **John S. Allen**[2], **Noriko Yanaba**[2], **Shelton D. Caruthers**[2], **Gregory M. Lanza**[2], **Marc R. Hammerman**[2], and **Samuel A. Wickline**[1,2,*]

[1]Department of Physics, Washington University in St. Louis, MO, 63130, USA

[2]Department of Medicine, Washington University in St. Louis, MO, 63130, USA

Abstract

Purpose—We sought to develop a unique sensor-reporter approach for functional kidney imaging that employs circulating perfluorocarbon nanoparticles (PFC NPs) and ^{19}F MRI.

Methods—Because the detected ^{19}F signal intensity directly reflects local blood volume, and the ^{19}F R1 is linearly proportional to local blood oxygen content (pO2), ^{19}F spin density weighted and T1 weighted images were utilized to generate quantitative functional mapping in both healthy and ischemia-reperfusion (acute kidney injury, AKI) injured mouse kidneys. ^{1}H Blood-Oxygenation-Level-Dependant (BOLD) MRI was also employed as a supplementary approach to facilitate the compressive analysis of renal circulation and its pathological changes in AKI.

Results—Heterogeneous blood volume distribution and intrarenal oxygenation gradient were confirmed in healthy kidneys by ^{19}F MRI. In a mouse model of AKI, ^{19}F MRI, in conjunction with BOLR MRI, sensitively delineated renal vascular damage and recovery. In the cortico-medullary (CM) junction region, we observed 25% lower ^{19}F signal ($p<0.05$) and 70% longer ^{1}H T2* ($p<0.01$) in injured kidneys compared to contralateral kidneys at 24 hours after initial ischemia-reperfusion injury. We also detected 71% higher ^{19}F signal ($p<0.01$) and 40% lower ^{1}H T2* ($p<0.05$) in the renal medulla region of injured kidneys compared to contralateral kidneys.

Conclusion—With demonstrated superior diagnostic capability, functional kidney ^{19}F MRI using PFC NPs could serve as a new diagnostic measures for comprehensive evaluation of renal function and pathology.

Keywords

Fluorine; Kidney; Perfusion; Oxygenation; Blood Volume; Ischemia-Reperfusion

[*]Send correspondence to: Samuel A. Wickline, MD, C-TRAIN Group, Campus Box 8215, Washington University School of Medicine, St. Louis, MO 63108, USA, Phone: 314-454-8635, Fax: 314-454-5265, saw@wuphysics.wustl.edu.

Introduction

Renal ischemia is a primary pathology in acute kidney injury (AKI), a disease inflicted upto 7% of hospitalized patients with high mortality rate (1–2). AKI may acutely lead to intrarenal non-perfusion causing ischemic injury to renal endothelial cells and tubular epithelial cells. Even after reperfusion, the ischemic injury may persist several days due to inflammation-coagulation interactions induced capillary non-perfusion (3–6). This "extension-phase" of ischemia exerted negative impact on tubular epithelial cell regeneration so that may cause permanent damage to the global glomeruous filtration rate (GFR). Unfortunately, current evaluation of renal injury is based on detecting increased level of creatinine or other kidney injury markers, which provided limited information of intrarenal ischemia that usually occurred regionally (7–10). Non-invasive assessment of intrarenal perfusion will benefit early staging the disease as well as promptly evaluating therapeutic intervention to restore oxygen delivery to tubular cells (11).

Non-invasive medical imaging methods for assessing intrarenal perfusion is yet lacking. The current standard approaches entail bolus injection of exogenous contrast agents (e.g. iodinated compounds for CT, gadolinium chelates for MRI, etc.) followed by a series of image acquisitions to capture the first-pass dynamics of contrast agents flowing through the kidney (12–14). These imaging agents, however, requires renal clearance that could cause kidney overload and compromise kidney function (15). Using gadolinium agents as example, its slow and incomplete clearance from the kidney can lead to irreversible nephrogenic systemic fibrosis (16–17). The high risk of contrast-induced nephropathy limits application of diagnostic imaging procedures in clinics, especially to patients who already have kidney diseases (18–21).

Over the past two decades, several clinical MRI techniques have been proposed for measuring kidney function utilizing the native ^{1}H contrast from the blood (7,22–23). Specifically, Blood-Oxygenation-Level-Dependent (BOLD) MRI has been applied to map intrarenal oxygenation based on the susceptibility effect of intravoxel deoxyhemoglbin induced shortening of ^{1}H T2* (24). However, the BOLD readouts are sensitive to many factors such as blood volume, flow rate, and field inhomogeneity or hemorrahage induced susceptibility artifact. In fact, a recent study showed no correlation between kidney dysfunction and BOLD readout in chronic kidney diseases (25). Many questions therefore remains to be addressed before translating renal BOLD MRI to clinic. Arterial Spin Labeling (ASL) MRI has also been proposed for defining renal perfusion without the need of exogenous contrast media(26–27). The technique may provide an accurate and reproducible readout of renal perfusion. However, its low signal to noise ratio is a serious concern for clinical application. Given these limitations, recent advances suggested multi-parametric MRI using BOLD, ASL, and/or other techniques may provide a more accurate readout for detecting intrarenal perfusion defect (22,28–29).

We hypothesize that integrating ^{1}H BOLD MRI with ^{19}F MRI of perfluorocarbon (PFC) based nanoparticles (NPs) could provide a non-nephrotoxic and quantitative measure of intrarenal perfusion. PFC NPs are a class of clinically approved blood-substitute with no report of nephrotoxic effect (30). It comprises a hydrophobic PFC core encapsulated by a

lipid monolayer. With a nominal size of ~250 nm, PFC NPs are primarily limited to intravascular space unless the integrity of endothelial barrier was compromised (e.g. in tumor). PFC NPs are cleared by the retinoendothelial system and lungs (31), which is different form most other imaging agents that requires renal clearance and potentiates kidney failure (21).

The ^{19}F molecule of PFC provides a unique MR spectroscopic signature because there is no ^{19}F signal in physiological tissue. Many works from our group and others have shown that the PFC can be detected at sparse concentrations (picomolar) with ^{19}F MRI (32–33). The linear relationship between the ^{19}F signal intensity and PFC volume, as well as the linear relationship between ^{19}F longitudinal relaxation rate (R1 = 1/T1) and local oxygen tension (pO2) (34–35), have been utilized for in vivo assessment of blood volume and pO2 mapping, respectively (36–37). Compared to BOLD and ASL MRI, the advantage of ^{19}F MRI is that the readout of renal blood volume and pO2 does not need model-based assumptions. A major limitation of ^{19}F MRI, however, is that it requires long data acquisition time that typically extends several to tens of minutes. Thus, we propose that integrating fast ^{1}H BOLD MRI with quantitative ^{19}F MRI will provide a novel non-invasive measure of intrarenal perfusion.

The objective of this study is to develop a multi-nuclear ^{1}H/^{19}F MRI approach for functional renal imaging using rodents. We first demonstrated the feasibility of ^{19}F MR mapping of renal blood volume (RBV) and pO2 in healthy mouse kidneys. Subsequently, a mouse ischemia-reperfusion AKI model (38) was employed to evaluate the accuracy of the multi-nuclear MRI technique on assessing renal injury. In this animal model, transient ischemia directly causes damage to endothelial and tubular cells. After reperfusion, the inflammatory reponse induced extensive interaction between inflammation and coagulation (4) that adversely causes sustained medullary microvessel non-perfusion (9) and tubular ischemia (4,10,39). The renal damage causes continuously increasing of creatinine and blood urea nitrogen (BUN) that peaked at 24–48 hours after reperfusion (3,40). Our results suggested that ^{19}F MRI measured RBV and pO2 colocalized with ^{1}H BOLD MRI revealed increased T2* in the cortical-medullary (CM) junction.

Methods

All animal procedures have been approved by the Animal Studies Committee of Washington University in St. Louis.

Nanoparticle formulation and calibration of ^{19}F R1 vs pO2

Perfluoro-15-crown-5-ether (CE) nanoparticles (NPs) were formulated as previously described (33). Briefly, the CE emulsion comprises 40% (v/v) of CE (Exfluor Research Corp., USA), 2.0% (w/v) of a surfactant commixture, and 1.7% (w/v) glycerin, in distilled water. CE NP was co-labeled with Alexa Fluor 594 for ex vivo fluorescence microscopy examination. In vitro calibration of ^{19}F R1 as a function of pO2 was performed at three different O_2 concentrations (0%, 21%, and 100% O_2 balanced with N_2) by bubbling gas mixtures into a CE emulsion sample for 30 minutes at 37°C. ^{19}F T1 measurements were

made at 11.7 T with inversion recovery spectroscopy at TR=10 s, with 10 inversion delays (TI) ranging from 3 ms to 5 s.

Mouse AKI model

C57/Bl6 mice (n=10) underwent laparotomy and a standard procedure to produce warm ischemia-reperfusion injury (41). Briefly, mice were anesthetized with ketamine/xylazine followed by a mid-line incision on the abdomen. After exposing the vasculature of the left kidney, we induced ischemia by ligating both renal artery and vein with a suture. Cessation of renal blood flow and restoration of perfusion after releasing the ligatures were confirmed visually by noting the color change of the kidneys. Mice with incomplete ischemia or reperfusion were excluded prospectively from the study. Ischemia was maintained for 60 minutes, during which mice were kept warm with a water-circulating blanket at 37°C. To avoid dehydration of exposed organs, warm saline was added to the abdominal cavity during ligation. 24 hours after surgery, both injured and contralateral kidneys were scanned with functional ^{19}F and BOLD MRI in vivo as described previously. After in vivo MRI, 10 μl FITC-lectin (Vector Laboratory, USA) was injected into the left ventricle and allowed to circulate for 5 minutes. Both kidneys were harvested and frozen in OCT media (Tissue-Trek, Japan) for fluorescence microscopic imaging and histological preparation.

In vivo ^{19}F and BOLD MRI of kidney

Mice were anesthetized with a continuous intramuscular infusion of ketamine/xylazine. Body temperature was monitored and maintained at 37 ± 1°C during the MRI scans with the use of a small animal monitoring system (SAI Inc., USA) and a feedback controlled heated fan system. Mice were restrained in a custom-built holder and allowed to breathe pure oxygen through a nose cone. The respiratory signal was acquired from additional tubing connected to the nose cone and used as the gating trigger for in vivo imaging.

All in vivo imaging was performed on an 11.7 T Varian scanner with a custom-built actively decoupled transmit/receive coil pair. Mice were placed in a supine position and the surface receive coil (size = 1 × 2 cm) was adjusted to match the mouse body curvature. The volume transmit coil (diameter = 5 cm , length = 10 cm) cover the entire mouse body to achieve a homogeneous B1 field in the imaging field of view, i.e. two kidneys. Both transmit and receive coils were tuned and matched at ^{19}F frequency for both ^{19}F and ^{1}H imaging. Because of the strong magnetization at the high field strength, the ^{1}H signal was sufficient to generate anatomical images within a minute despite RF coils are off-resonance.

Before in vivo MRI, 0.1 mL (~ 5mL/Kg) CE NP was administrated intravenously through the tail vein. A ^{1}H gradient echo sequence was employed to locate the region of interest (ROI) followed by a ^{1}H multi-echo gradient echo BOLD scan with: TR = 100 ms, TE = 1.96 ms with 1.75 ms increment for every echo, flip angle = 10°, field of view = 26 mm × 26 mm, voxel size = 0.2 mm × 0.2 mm × 2 mm. Two imaging slices with 2 mm thickness were positioned 1–2 mm apart and centered at left and right kidney, respectively. Two sets of ^{19}F MRI scans (spin density weighted and T1-weighted images) were performed using a respiration-gated fast spin echo sequence. TR was set to 4 s for the spin density weighted ^{19}F MRI whereas the TR was set to two respiration periods (e.g. ~300 ms) for the

T1-weighted imaging. All other imaging parameters are identical in these two sets of ^{19}F MRI: ETL = 4, TE = 11.5 ms, receive bandwidth =20 kHz, voxel size = 0.4 mm × 0.4 mm × 2 mm, and the field of view identical for ^{1}H scout and BOLD imaging. Different anatomical regions, including renal cortex, CM junction and renal medulla were manually segementated on T2*-weighted images and copied over to both sets of ^{19}F images. The spatial localization and distribution of all three anotomial areas were selected so as to be consistent with previous reports of BOLD MRI on mouse kidneys (41–43) .

Quantification of ^{19}F singal intensity and intrarenal pO2

A RF coil sensitivity map was acquired using a saline phantom positioned at the selected imaging location. Imaging parameters were: TR = 100 ms, TE = 1.96 ms, and flip angle = 10°. At spatial location [x,y,z], the phantom image defines a correction factor $R(x, y, z)$, i.e. the inverse of local signal intensity. By multiplying $R(x, y, z)$ with in vivo measured image signal intensity at the corresponding location, the spatial inhomogeneity of RF coil sensitivity profile could be compensated (44):

$$S=\frac{S_{long}(x,y,z)\times R(x,y,z)}{S_{long}(x_0,y_0,z_0)\times R(x_0,y_0,z_0)}, \quad [1]$$

where $S_{long}(x, y, z)$ and $S_{long}(x_0, y_0, z_0)$ are the signal intensities at the kidney and the external standard in the ^{19}F spin density weighted images. $R(x, y, z)$ and $R(x_0, y_0, z_0)$ are the correction factors at the location of kidney and the external standard. In healthy tissues, PFC NPs are constrained inside the intravascular space because of their large particle size, therefore the measured ^{19}F signal intensity linearly correlates with absolute blood volume (34).

In vivo renal T1 quantification and pO2 measurement were based on the general assumption that image signal intensity in a fast spin echo sequence follows a saturation-recovery process and is determined by TR:

$$S(TR)=S_0(1-e^{-TR/T1}), \quad [2]$$

where S_0 is a TR-independent baseline parameter. This approximation is accurate to the first order when TE << TR in a fast spin echo sequence (45). In the present study, TR for spin density and T1-weighted images were 4 s and ~1 s respectively (or ~400 and ~100 times longer than TE = 11.5 ms, respectively). Therefore, Eq. [2] was applicable for approximating the signal intensity in renal ^{19}F images.

Because T1-weighed ^{19}F MRI was gated with respiration (rate = 100 – 150 min^{-1}or 1.7 – 2.5 s^{-1}), the real TR might vary from animal to animal. The animal respiration rate is 100–150 min^{-1}. Given the ^{19}F T1 of PFC standard is 0.9 s-1 s at room oxygen tension (Fig. 1), the signal acquired with TR = 4 s, i.e. > 3 T_1, should approximate the ^{19}F spin-density signal of PFC NP. Thus, the real TR_{short} was determined using the external standard based on its pre-calibrated T1 ($T1_{std}$) and its ^{19}F signal intensity acquired at TR = 4 s (S_{long}):

$$TR_{short} = -T1_{std} \times \ln\left(\frac{S_{short}(x_0, y_0, z_0)}{S_{long}(x_0, y_0, z_0)}\right), \quad [3]$$

where S_{short} is the signal acquired when TR was set at 1s.

Once the real TR_{short} was determined using the external standard, voxel-wise T1 mapping of the kidney could be achieved by

$$T1(x, y, z) = \frac{TR_{short}}{\ln(S_{long}(x, y, z)) - \ln(S_{short}(x, y, z))}. \quad [4]$$

Finally, T1 values were translated into corresponding pO2 levels according to the pre-determined calibration curve (Fig. 2c).

The consistency of ^{19}F and T1 quantification methodology was also evaluted in vivo on healthy mice (n = 5).

Validation of ^{19}F T1 quantification

We performed a phantom study to validate the accuracy of Eq. [1] and [2]. Briefly, five 1 ml syringes containing 40%, 4%, 40%, 10% and 20% volume concentrations of CE NP were placed at locations 1–5 (Fig. 1) in the animal holder. The same fast spin-echo protocol for in vivo imaging was utilized and the same correction factor Rx, y, z) from sensitivity mapping was applied to the acquired images to correct for the receiving inhomogeneity. TR value changed from 0.1 s to 8 s to evaluate the approximation of saturation recovery signal as described in Eq. [2].

To confirm that the selection of TR = 4s in the proposed imaging protocol was optimal for ^{19}F quantification and caused no additional deviation to the measurement of RBV, we acquired two consecutive images of kidneys at the identical location with TR=4s and 8s respectively. Experiment was repeated at three different animals and the signal difference between images with different TR values was used to evaluate the potential impact of non-fully recovered magnetization on kidney ^{19}F imaging.

Because the T1-weighted and spin density weighted ^{19}F images were acquired consecutively but at slightly different time point, we experimentally validated that the impact of pharmacokinetic clearance of PFC NP on RBV and pO2 results was minimal. Specifically, ^{19}F signal intensity at both kidney and spleen was measured over time (from 1 hour to 3 hours) in two imaging subjects. The ^{19}F signal at kidneys was modeled as exponential decay because it is caused by the clearance of PFC NP in the blood stream (37). The fitted half life time of ^{19}F signal at kidneys were used to evaluate the potential signal change over in vivo RBV and pO2 measurement.

Histology and fluorescence imaging

Frozen tissues were sectioned into 8 μm slices for histology and fluorescence imaging. Briefly, hematoxylin and eosin were used to stain kidneys to confirm tissue damage caused

by ischemia-reperfusion. Fluorescence images were digitized with an Olympus BX61 fluorescent microscope after mounting with DAPI mount media (Vectashield Inc., USA). DAPI, Texas Red and FITC channels were selected to image the nucleus, CE NP, and perfused blood vessels respectively. All fluorescence images were color coded and co-registered in IMAGEJ (NIH, USA).

Data processing and statistics

All MRI images and signal analyses were processed with a custom-designed program written in Matlab (MathWorks, USA). Segmentation for different regions in healthy kidneys was performed manually based on ^{19}F spin density weighted and ^{1}H T2* weighted images. All statistical analyses were conducted in Origin (OriginLab, USA): paired t-tests and repeated measures ANOVA were used for hypothesis testing as indicated.

Results

Validation of quantitative ^{19}F MRI measurement

Figure 1a shows the RF sensitivity map of the surface coil. Before signal correction, ^{19}F signal in individual CE NP phantom was inhomogenous (Fig. 1b). After sensitivity correction using Eq. [1], improved signal homogeneity and accuracy of quantified CE NP concentration was visually appreciable (Fig. 1c). Using phantom 4 as a reference standard, the pre-correction ^{19}F MRI measured CE NP concentration in phantom 1–3, and 5 deviated from their real value by 5%, 28%, 17%, and 11%, respectively. After signal correction, the error of quantified CE NP concentration decreased to 3%, 15%, 7%, and 10%, respectively. The fitted T1 values in phantoms 1 – 5 were 0.90 s, 0.89 s, 0.98 s, 0.87 s and 0.94, respectively($R > 0.99$ for all fittings). As expected, these T1 values matched to each other despite differences in PFC NPs concentration.

Figure 2a shows blood clearance of PFC NPs induced longitudinal changes of ^{19}F MR signal intensity in mouse kidneys and spleen. The ^{19}F signal in the spleen steadily increased due to its retention of CE NPs from blood (37). Despite of the blood clearance, the recorded ^{19}F signal of circulating PFC NPs in kidney shows a fitted blood half-life of 426 min, suggesting the ^{19}F signal decay during the time course of in vivo imaging may be insignificant (30 min). Figure 2b shows the difference of ^{19}F signal intensity in mouse kidney was 3 ± 1% when acquired consequetively with TR = 8s and 4s, suggesting TR = 4s is sufficient for ^{19}F spin-density imaging due to replenishing of renal blood.

Figure 2c shows the linear dependence of ^{19}F R1 on pO2. At 37 °C, the calibrated linear relationship between ^{19}F R1 (=1/T1) and pO2 was :

$$R1(s^{-1}) = (0.0032 \pm 0.0001) \times pO_2(mmHg) + (0.72 \pm 0.02), \quad [5]$$

The correlation coefficient $R > 0.99$.

^{1}H and ^{19}F MRI of healthy kidneys

Figure 3 shows representative ^{1}H T1-weighted, ^{1}H T2*-weighted, ^{19}F spin density weighted, and ^{19}F T1-weighted images of kidneys in healthy mice. Compared to the ^{1}H T1-

weighted image (Fig. 3a), the signal intensity of medulla was lower on the ^{1}H T2*-weighted image (Fig. 3b) reflecting its higher ratio of dexoyhemoglibin under physiological conditions. ^{19}F spin-density image (Fig. 3c) shows the ^{19}F signal intensity decreased from the cortex to the CM junction reflecting intra-renal perfusion (Fig. 3c). In the inner portion of kidney that contains not only medullary microvasculature but also major renal artery/vein, high ^{19}F signal was detected. In this study, the CM junction that presents the outer medulla and inner side of the cortex, the cortex,and the medulla was selected as ROI for data analysis (Fig. 3c, insert). The ^{19}F signal contrast between cortex and CM junction was enhanced by T1-weighting due to a relative decrease of T1-weighed signal in the CM junction(Fig. 3d), reflecting longer ^{19}F T1 relaxation recovery in this nearly hypoxic region (11).

Heterogeneous distribution of ^{19}F intensity and intrarenal oxygenation was confirmed by quantitative mapping of ^{1}H T2*, ^{19}F spin-density signal, and ^{19}F T1 derived pO2 as illustrated in Fig. 4(a–c) and summarized in Fig. 4(d–f). ^{1}H BOLD MRI detected longer ^{1}H T2*, indicating higher tissue oxygenation (24) in renal cortex than the CM junction. In the inner medulla, however, BOLD MRI showed longer ^{1}H T2* , which has been previously recognized as a technical limitation of renal BOLD MRI (42). ^{19}F spin-density maps revealed inhomogeneous regional blood supply in healthy kidneys (46). Using Eq. [5], intrarenal pO2 was derived by in vivo ^{19}F MRI quantified T1. The quantified pO2 was 361±67 mmHg in the renal cortex that is substantially higher than the 138 ± 66 mmHg pO2 in the CM junction ($p < 0.05$). The ^{19}F MRI detected pO2 in inner medulla was 30 ± 20 mmHg.

^{1}H and ^{19}F MRI of ischemia-reperfusion injured kidneys

Upon the completion of MRI assessment of renal oxygenation and perfusion in kidneys of normal mice, we applied the same techniques to evaluate renal injury at 24 hours after unilateral (left) renal ischemia-reperfusion. BOLD MRI detected abnormal T2* signal enhancement in the CM junction of injured kidneys (Fig. 5). T2* of ^{1}H in CM junction increased approximately 70% ($p<0.01$, Fig. 6). Subsequent ^{19}F MRI showed pO2 in the CM junction remained largely unchanged. Instead, ^{19}F signal decreased approximately 25% ($p < 0.05$) reflecting reduced blood volume in CM junction. In the renal cortex, ^{1}H T2*, ^{19}F signal quantificaiton, and pO2 of injured kidneys were all comparable to those of contralateral control kidneys, suggesting recovery of perfusion and oxygenation in this region. In the inner medulla, however, vascular leakage and hemorrhage-induced extravascular retention of PFC NPs (Fig. 7) resulted in a pseudo readout of reduced ^{1}H T2* ($p<0.05$), increased ^{19}F signal intensity ($p<0.01$), and unchanged pO2.

Histology and fluorescence image

Endothelial staining with FITC-lectin demonstrated the reduced density of perfused blood vessel in the CM junction (Fig. 7a). Fluorescence microscopy of PFC NP confirmed the accumulation of PFC NP within the renal medulla in comparison to the uninjured contralateral kidneys (Fig. 7b). By co-registering the FITC-lectin endothelial staining with the fluorescent PFC NP (Fig. 7c), we observed that PFC NP accumulated within extravascular spaces in injured kidneys, suggesting that the high PFC NP concentration in the renal medulla could be attributed to vascular leakage that developed after ischemia-

reperfusion. Finally, H&E staining revealed extensive tissue damage and necrosis at the CM junction and in the medulla regions of injured kidneys (Fig. 8).

Discussion and Conclusions

Intrarenal non-perfusion is a primary pathology of AKI. The restoration of renal blood flow activates inflammatory-coagulation interactions that adversely causes non-perfusion of capillaries and micro-vessels. The resulted insufficient oxygen delivery leads to sustained ischemic injury to tubular cells, i.e. the “extension phase” of AKI (47). Intrarenal non-perfusion was found to be more severe in the renal medulla and CM junction than in the cortex (4,8,39). Unfortunately, non-invasive methods for in vivo assessment of intrarenal non-perfusion after AKI is lacking.

The sensitivity of ^{1}H BOLD MRI to renal perfusion defects and its limitation has been extensively investigated in previous studies. The hypothesis of ^{1}H BOLD MRI is that increased concentration paramagnetic deoxyhemoglobin augments susceptibility effect and causes decreased T2*. A major limitation of renal BOLD MRI, however, is that T2* is affected by many other factors including blood volume and hemoglobin concentration. To use T2* as a readout of pO_2, the volume of blood vessels in voxels of injured kidney need to be the same in voxels to be compared (48–49). This assumption is unlikely to hold in AKI due to massive intrarenal microvessel nonperfusion, nor in chronic kidney diseases in which renal vessel atrophy could occur (8,50). Thus, despite BOLD MRI could sensitively detect abnormal T2* in diseased kidneys, the underlying tissue pathology is yet unclear that greatly challenged its clinical transaltion (48).

The novelty of this multi-nuclear functional kidney imaging approach is that it integrated the sensitivy of ^{1}H BOLD MRI to renal injury with the quantifiable properties of ^{19}F signal from circulating PFC NPs to evaluate intrarenal blood volume and pO2. As an blood-pool agent, the volume of PFC NPs directly represents the volume of blood and can be quantified by the ^{19}F signal intensity in each voxel. In addition, ^{19}F R1 (=1/T1) of PFC NPs is linearly responsive to local oxygen tension over a wide range of values (35–36). Since the oxygen exchange between blood and PFC NPs occurs by free diffusion at millisecond time scale (51), the measured pO2 from PFC NPs represents the pO2 of surrounding blood. Thus, combining ^{1}H BOLD MRI, spin density ^{19}F MRI and ^{19}F T1 measurement provides multi-parametric readouts for in vivo assessmen of renal blood volume and pO2.

The measured regional distribution of blood volume as represented by ^{19}F signal intensity and oxygenation in normal kidneys is consistent with previously reported values using ex-vivo (52) and invasive measurements (11,53–55). Renal blood vessel has unique distribution resulting inhomogeneous tissue oxygenation. Renal artery/vein branches and penetrates through medulla to the cortex. The majority of renal blood flow then goes through glomerular filtration in the renal cortex. Only a small portion of renal blood supports to the capillary beds in CM junction and inner medulla, resulting in an a steep oxygenation gradient from renal cortex to medulla. Accordingly, ^{19}F MRI detected pO2 was the highest in the cortex and the lowest in the inner medulla in heathy kidneys (Fig. 5).

In the mouse model of renal ischemia-reperfusion injury, the employed multi-nuclear MRI approach successfully detected reperfusion defects in the CM junction. Specifically, ^{1}H BOLD MRI sensitively revealed abnormal high T2*, reflecting reduced susceptibility effect that may attribute to decreased ratio of deoxyhemoglibin and/or reduced blood flow (56). Using ^{19}F MRI, a reduction of spin-density ^{19}F signal was observed in the same region indicating reduced blood volume. Agreeing with ^{19}F MRI observations, histology revealed lower density of perfused blood vessels. Finally, ^{19}F T1 derived blood pO2 exhibited no significant change. Taken together, our data suggested that insufficient perfusion in the CM junction reduces the susceptibility effect resulting in increased ^{1}H T2*. In the renal cortex, ^{1}H BOLD MRI determined T2*, ^{19}F MRI determined blood volume and pO2 all recovered to baseline value, reflecting less severe vascular damage in this region (8–9,47). In inner medulla of injured kidney, however, ^{19}F MRI does not necessarily correlates with RBV. As confirmed by histology analysis, there is massive extravascular accumulation of PFC NP in inner medulla (norminal size = 250 nm), reflecting ischemia-reperfusion injury induced vascular leakage or hemorrhage during extension phase of AKI (57). These trapped PFC NPs causes high ^{19}F signal intensity that may falsely representing high blood volume.

To estimate ^{19}F T1 of flowing PFC NPs in renal blood, the current study employed traditional T1-weighted saturation-recovery techniques instead of fast ^{19}F T1 measurement methods, such as Fredom and SNAP-IR sequences developed by other groups and the BESR sequence developed by our lab (58–60). The Fredom and SNAP-IR sequences are optimized for imaging stationary PFC NPs stationarized in regions of interest (e.g. injected into tumor). The imaging sequence comprises a single excitation/inversion recover pulse followed by a pulse-echo train sampling during the T1 recovery. Because there is no moving effect from PFC NPs, the ^{19}F T1 could be accurately estimated by modeling perturbations from sequential RF pulses. However, to apply these techniques to flowing PFC NPs, the in-flow and out-flow induced continuous refreshing of spins at each pulse-echo need to counted into the model, which is yet unavailable, or a homogeneous global spin excitation to cover blood in whole body will be needed that may cause excessive SAR. The BESR sequence developed by our group utilizes a global saturation followed by multiple gradient echoes. It is optimized for quantifying ^{19}F T1 of flowing PFC NPs in major blood vessels so that a complete refreshing of ^{19}F spins is achieved before each ECG gated gradient-echo. The BESR sequence is not appropriate for measuring ^{19}F T1 of the slow moving PFC NPs in renal capillaries. Thus, in this study standard T1-weighted images were selected for in vivo quantification of ^{19}F T1.

Compared to traditional contrast agents for imaging renal perfusion, PFC NPs has a good clinical safey profile. It is cleared from circulation by the reticuloendothelial system and progressively released back to blood and evaporized through lungs. No renal toxicity in animals or human has been reported. PFC NPs have been used in both animals and humans for various purposes including oxygen delivery, contrast enhanced imaging, and stem cell tracking. Currently, a PFOB based PFC NPs is under Phase I clinical trial in our lab for imaging atherosclerotic plaques.

The proposed multi-nuclear protocol utilizing intraveneously injection of PFC NPs is clinically translatable. The unique ^{19}F signal emanating from the PFC moieties in the core of

the nanoparticle can be detected readily with ^{19}F MRI on both research and clinical scanners, such as the Philips 3T clinical scanners equipped with ^{19}F signal acquisition system that is operating in many sites including our center. Using the broad-band imaging technique developed by our group (61), the same PFOB NPs may be used for renal imaging in human. We anticipate that fully optimized imaging protocols would enable the entire procedure of ^{1}H/^{19}F functional kidney imaging to be conducted within a clinically relevant time frame (<30 minutes in the present study). If successful, this clinically translatable renal imaging technique provides functional renal imaging in AKI patients.

Limitations

The current study employs a slice-selective sequence to assess ^{19}F T1 of circulating PFC NPs. Because of blood flow induced partial refreshing of unexcited spins between adjacent echoes, the detected T1-weighted signal recovers faster than the real T1 recovery of excited spins. The resulted underestimation of T1 is demonstrated by the equivalent ^{19}F signal intensity between TR = 4s and 8s (Fig. 2b) despite the ^{19}F T1 at pO2 = 0 mmHg is ~2s (Fig. 2c).

^{19}F MRI measurement of blood volume is based on the assumption that PFC NPs is homogeneously distributed in the blood pool. The detected ^{19}F signal intensity in spin-density images therefore directly reflects RBV in normal kidney vessels. After ischemia-reperfusion, however, transient vascular leakage developed that was shown to be most severe in the inner medulla (Fig. 8b). Because of the extravsation of blood cells and PFC NPs, neither ^{1}H BOLD MRI nor ^{19}F MRI is reliable for in vivo imaging medullary perfusion deficiency, which presents a limitation for this study. Thus, accurate MRI readout perfusion in the mouse AKI model is limited to the cortex and the CM junction.

The current study employs slice-selective sequence to assess ^{19}F T1 of circulating PFC NPs. Due to blood flow induced partial refreshing of unexcited spins between adjacent echoes, the detected T1-weighted signal recovers faster than the real T1 recovery of excited spins. The resulted shorter estimated T1 is demonstrated by the equivalent ^{19}F signal intensity between TR = 4s (< 3 T1) and 8s despite the ^{19}F T1 in venous blood is ~2s. Alternatively, for spin-density image that employs long TR, the residue excitation from previous echo may lead to underestimation of ^{19}F signal intensity. However, since the average mouse blood volume is 1.7 mL and cardiac output is 8.0 mL/min, the time for an excited spins to flow back to kidney is 1.7/8*60 ~= 13s (> 3 T1), suggesting fully recovery of spins' magnetization when they reflow back to kidneys.

A mono-exponential T1 recovery model is used to fit ^{19}F T1 of PFC NPs and to derive blood pO2. Given blood pO2 changes continuously from artery to capillary to vein, the ^{19}F T1 of circulating PFC NPs will also exhibit a continuous distribution between 1 s (arterial T1) and 2 s (venous T1) (Fig. 2c). However, due to the faster arterial flow induced faster decay of spin echo signal (the "black-blood" effect), the detected ^{19}F signal should mostly attribute to slow moving spins in capillaries and veins so that reflects intrarenal oxygen consumption. More sophisticated models using multi-compartment and multi-exponential fitting may improve the accuracy of pO2 measurement but requires experimental validations.

It is known that anesthesia alters circulation from its normal physiological settings, which is a general concern for MRI of experimental animal models. In addition, paramagnetic deoxygenated hemoglobin generates strong local field inhomogeneities at 11.7 T that significantly reduce the signal to noise ratio of ^{19}F MR image. To mitigate this effect, quantitative mapping of renal blood volume and oxygenation were performed only when mice were breathing pure oxygen, which will adversely cause vessel constriction that reduces renal blood volume (62). To minimize these effects, a unilateral AKI model was employed so that the contralateral non-injured kidney in each mouse provides a paired internal control. In addition, all animals were imaged under the same experimental settings. Our results showed the in vivo MRI detected regional renal perfusion deficiency agreed with histological observations despite the above mentioned experimental limitations.

Other limitations are: 1) experiments were performed at a single time point at 24 hours after ischemia-reperfusion when maximal damage to renal function occurred in rodent models (3,40). Further longitudinal studies to correlate in vivo MRI readout with renal function and histolopatholgy will be desirable to follow up the disease progression; 2) the limited temporal resolution of ^{19}F MRI currently poses an obstacle for capturing the first pass of the contrast agent. Therefore, dynamic parameters such as transient time and renal blood flow rate cannot be determined from these ^{19}F MRI measurements. Again, optimizations in pulse sequence and RF coil design and performance could ultimately enhance detection sensitivity and enable applications that require higher temporal resolution.

Acknowledgments

We thank Dan Martin for technical support on AKI surgery. We also thank Mark S. Conradi for helpful discussion. We acknowledge the financial support from AHA predoctoral fellowship to LH, NIH grant R01 HL073646 to SAW and NIH grant P30 DK079333 for Renal O'Brien Center at Washington University in St. Louis.

Reference

1. Hou SH, Bushinsky DA, Wish JB, Cohen JJ, Harrington JT. Hospital-acquired renal insufficiency: a prospective study. Am J Med. 1983; 74(2):243–248. [PubMed: 6824004]
2. Shusterman N, Strom BL, Murray TG, Morrison G, West SL, Maislin G. Risk factors and outcome of hospital-acquired acute renal failure. Clinical epidemiologic study. Am J Med. 1987; 83(1):65–71. [PubMed: 3605183]
3. Mizutani A, Okajima K, Uchiba M, Isobe H, Harada N, Mizutani S, Noguchi T. Antithrombin reduces ischemia/reperfusion-induced renal injury in rats by inhibiting leukocyte activation through promotion of prostacyclin production. Blood. 2003; 101(8):3029–3036. [PubMed: 12480701]
4. Basile DP. The endothelial cell in ischemic acute kidney injury: implications for acute and chronic function. Kidney Int. 2007; 72(2):151–156. [PubMed: 17495858]
5. Evans RG, Gardiner BS, Smith DW, O'Connor PM. Intrarenal oxygenation: unique challenges and the biophysical basis of homeostasis. Am J Physiol Renal Physiol. 2008; 295(5):F1259–F1270. [PubMed: 18550645]
6. Sutton TA, Fisher CJ, Molitoris BA. Microvascular endothelial injury and dysfunction during ischemic acute renal failure. Kidney Int. 2002; 62(5):1539–1549. [PubMed: 12371954]
7. Grenier N, Basseau F, Ries M, Tyndal B, Jones R, Moonen C. Functional MRI of the kidney. Abdom Imaging. 2003; 28(2):164–175. [PubMed: 12592462]
8. Lameire NH, Vanholder R. Pathophysiology of ischaemic acute renal failure. Best Pract Res Clin Anaesthesiol. 2004; 18(1):21–36. [PubMed: 14760872]

9. Mason J, Torhorst J, Welsch J. Role of the medullary perfusion defect in the pathogenesis of ischemic renal failure. Kidney Int. 1984; 26(3):283–293. [PubMed: 6513274]
10. Devarajan P. Update on mechanisms of ischemic acute kidney injury. J Am Soc Nephrol. 2006; 17(6):1503–1520. [PubMed: 16707563]
11. Brezis M, Rosen S. Hypoxia of the renal medulla--its implications for disease. N Engl J Med. 1995; 332(10):647–655. [PubMed: 7845430]
12. Kalantarinia K. Novel imaging techniques in acute kidney injury. Curr Drug Targets. 2009; 10(12): 1184–1189. [PubMed: 19715540]
13. Prasad PV. Functional MRI of the kidney: tools for translational studies of pathophysiology of renal disease. Am J Physiol Renal Physiol. 2006; 290(5):F958–F974. [PubMed: 16601297]
14. Tsushima Y. Functional CT of the kidney. Eur J Radiol. 1999; 30(3):191–197. [PubMed: 10452717]
15. Aparicio LS, Boggio GF, Waisman GD, Romero JC. Advances in noninvasive methods for functional evaluation of renovascular disease. J Am Soc Hypertens. 2009; 3(1):42–51. [PubMed: 20409944]
16. Sadowski EA, Bennett LK, Chan MR, Wentland AL, Garrett AL, Garrett RW, Djamali A. Nephrogenic systemic fibrosis: risk factors and incidence estimation. Radiology. 2007; 243(1): 148–157. [PubMed: 17267695]
17. Boyd AS, Zic JA, Abraham JL. Gadolinium deposition in nephrogenic fibrosing dermopathy. J Am Acad Dermatol. 2007; 56(1):27–30. [PubMed: 17109993]
18. Gleeson TG, Bulugahapitiya S. Contrast-induced nephropathy. AJR Am J Roentgenol. 2004; 183(6):1673–1689. [PubMed: 15547209]
19. Wong PC, Li Z, Guo J, Zhang A. Pathophysiology of contrast-induced nephropathy. Int J Cardiol. 2012; 158(2):186–192. [PubMed: 21784541]
20. Briguori C, Visconti G, Focaccio A, Airoldi F, Valgimigli M, Sangiorgi GM, Golia B, Ricciardelli B, Condorelli G. Renal Insufficiency After Contrast Media Administration Trial II (REMEDIAL II): RenalGuard System in high-risk patients for contrast-induced acute kidney injury. Circulation. 2011; 124(11):1260–1269. [PubMed: 21844075]
21. Briguori C, Marenzi G. Contrast-induced nephropathy: pharmacological prophylaxis. Kidney Int Suppl. 2006; (100):S30–S38. [PubMed: 16612399]
22. Ries M, Basseau F, Tyndal B, Jones R, Deminiere C, Catargi B, Combe C, Moonen CW, Grenier N. Renal diffusion and BOLD MRI in experimental diabetic nephropathy. Blood oxygen level-dependent. J Magn Reson Imaging. 2003; 17(1):104–113. [PubMed: 12500279]
23. Maril N, Rosen Y, Reynolds GH, Ivanishev A, Ngo L, Lenkinski RE. Sodium MRI of the human kidney at 3 tesla. Magnetic Resonance in Medicine. 2006; 56(6):1229–1234. [PubMed: 17089361]
24. Prasad PV, Edelman RR, Epstein FH. Noninvasive evaluation of intrarenal oxygenation with BOLD MRI. Circulation. 1996; 94(12):3271–3275. [PubMed: 8989140]
25. Pruijm M, Hofmann L, Vogt B, Muller ME, Piskunowicz M, Stuber M, Burnier M. Renal tissue oxygenation in essential hypertension and chronic kidney disease. Int J Hypertens. 2013; 2013:696598. [PubMed: 23509612]
26. Detre JA, Zhang WG, Roberts DA, Silva AC, Williams DS, Grandis DJ, Koretsky AP, Leigh JS. TISSUE-SPECIFIC PERFUSION IMAGING USING ARTERIAL SPIN-LABELING. Nmr in Biomedicine. 1994; 7(1–2):75–82. [PubMed: 8068529]
27. Liu YP, Song R, Liang C, Chen X, Liu B. Arterial spin labeling blood flow magnetic resonance imaging for evaluation of renal injury. Am J Physiol Renal Physiol. 2012; 303(4):F551–F558. [PubMed: 22647631]
28. Wu WC, Su MY, Chang CC, Tseng WY, Liu KL. Renal perfusion 3-T MR imaging: a comparative study of arterial spin labeling and dynamic contrast-enhanced techniques. Radiology. 2011; 261(3):845–853. [PubMed: 22095996]
29. Chandarana H, Lee VS. Renal Functional MRI: Are We Ready for Clinical Application? American Journal of Roentgenology. 2009; 192(6):1550–1557. [PubMed: 19457818]
30. Spahn DR. Blood substitutes. Artificial oxygen carriers: perfluorocarbon emulsions. Crit Care. 1999; 3(5):R93–R97. [PubMed: 11094488]

31. Cohn CS, Cushing MM. Oxygen therapeutics: perfluorocarbons and blood substitute safety. Crit Care Clin. 2009; 25(2):399–414. Table of Contents. [PubMed: 19341916]
32. Partlow KC, Chen J, Brant JA, Neubauer AM, Meyerrose TE, Creer MH, Nolta JA, Caruthers SD, Lanza GM, Wickline SA. 19F magnetic resonance imaging for stem/progenitor cell tracking with multiple unique perfluorocarbon nanobeacons. FASEB J. 2007; 21(8):1647–1654. [PubMed: 17284484]
33. Neubauer AM, Caruthers SD, Hockett FD, Cyrus T, Robertson JD, Allen JS, Williams TD, Fuhrhop RW, Lanza GM, Wickline SA. Fluorine cardiovascular magnetic resonance angiography in vivo at 1.5 T with perfluorocarbon nanoparticle contrast agents. J Cardiovasc Magn Reson. 2007; 9(3):565–573. [PubMed: 17365236]
34. Rottman GA, Judd RM, Yin FC. Validation of 19F-magnetic resonance determination of myocardial blood volume. Magn Reson Med. 1995; 34(4):628–631. [PubMed: 8524033]
35. Mason RP. Non-invasive physiology: 19F NMR of perfluorocarbons. Artif Cells Blood Substit Immobil Biotechnol. 1994; 22(4):1141–1153. [PubMed: 7849916]
36. Mason RP, Nunnally RL, Antich PP. Tissue oxygenation: a novel determination using 19F surface coil NMR spectroscopy of sequestered perfluorocarbon emulsion. Magn Reson Med. 1991; 18(1): 71–79. [PubMed: 2062243]
37. Wickline, SA.; Mason, RP.; Caruthers, SD.; Chen, J.; Winter, PM.; Hughes, MS.; Lanza, GM. Fluorocarbon agents for multimodal molecular imaging and targeted therapeutics. In: Weissleder, R.; Ross, BD.; Rehemtulla, A.; Gambhir, SS., editors. Molecular imaging: Principles and practice: Peoples Medical Publishing House-USA. 2010. p. 542-573.
38. Paller MS, Murray BM. Renal dysfunction in animal models of cyclosporine toxicity. Transplant Proc. 1985; 17(4 Suppl 1):155–159. [PubMed: 3895656]
39. Basile DP, Donohoe D, Roethe K, Osborn JL. Renal ischemic injury results in permanent damage to peritubular capillaries and influences long-term function. Am J Physiol Renal Physiol. 2001; 281(5):F887–F899. [PubMed: 11592947]
40. Miller SB, Martin DR, Kissane J, Hammerman MR. Insulin-like growth factor I accelerates recovery from ischemic acute tubular necrosis in the rat. Proc Natl Acad Sci U S A. 1992; 89(24): 11876–11880. [PubMed: 1465411]
41. Oostendorp M, de Vries EE, Slenter JM, Peutz-Kootstra CJ, Snoeijs MG, Post MJ, van Heurn LW, Backes WH. MRI of renal oxygenation and function after normothermic ischemia-reperfusion injury. NMR Biomed. 2011; 24(2):194–200. [PubMed: 20954164]
42. Prasad PV. Evaluation of intra-renal oxygenation by BOLD MRI. Nephron Clin Pract. 2006; 103(2):c58–c65. [PubMed: 16543757]
43. Li LP, Ji L, Lindsay S, Prasad PV. Evaluation of intrarenal oxygenation in mice by BOLD MRI on a 3.0T human whole-body scanner. J Magn Reson Imaging. 2007; 25(3):635–638. [PubMed: 17279536]
44. Wijnen JP, van der Kemp WJ, Luttje MP, Korteweg MA, Luijten PR, Klomp DW. Quantitative (31) P magnetic resonance spectroscopy of the human breast at 7 T. Magn Reson Med. 2012; 68(2):339–348. [PubMed: 22213214]
45. Meara SJ, Barker GJ. Evolution of the longitudinal magnetization for pulse sequences using a fast spin-echo readout: application to fluid-attenuated inversion-recovery and double inversion-recovery sequences. Magn Reson Med. 2005; 54(1):241–245. [PubMed: 15968670]
46. Vander, AJ.; Pooler, J.; Eaton, DC. Lange physiology series. New York, NY: Lange Medical Books/McGraw Hill, Medical Pub. Division; 2004. Vander's renal physiology; p. v
47. Molitoris BA, Sutton TA. Endothelial injury and dysfunction: role in the extension phase of acute renal failure. Kidney Int. 2004; 66(2):496–499. [PubMed: 15253696]
48. Evans RG, Leong CL, Anderson WP, O'Connor PM. Don't be so BOLD: Potential limitations in the use of BOLD MRI for studies of renal oxygenation. Kidney Int. 2007; 71(12):1327–1328. [PubMed: 17554358]
49. He X, Yablonskiy DA. Quantitative BOLD: mapping of human cerebral deoxygenated blood volume and oxygen extraction fraction: default state. Magn Reson Med. 2007; 57(1):115–126. [PubMed: 17191227]

50. Recio-Mayoral A, Banerjee D, Streather C, Kaski JC. Endothelial dysfunction, inflammation and atherosclerosis in chronic kidney disease--a cross-sectional study of predialysis, dialysis and kidney-transplantation patients. Atherosclerosis. 2011; 216(2):446–451. [PubMed: 21414625]
51. O'Brien RN, Langlais AJ, Seufert WD. Diffusion coefficients of respiratory gases in a perfluorocarbon liquid. Science. 1982; 217(4555):153–155. [PubMed: 6806902]
52. Bentley MD, Ortiz MC, Ritman EL, Romero JC. The use of microcomputed tomography to study microvasculature in small rodents. Am J Physiol Regul Integr Comp Physiol. 2002; 282(5):R1267–R1279. [PubMed: 11959666]
53. Welch WJ, Baumgartl H, Lubbers D, Wilcox CS. Nephron pO2 and renal oxygen usage in the hypertensive rat kidney. Kidney Int. 2001; 59(1):230–237. [PubMed: 11135075]
54. Evans RG, Gardiner BS, Smith DW, O'Connor PM. Methods for studying the physiology of kidney oxygenation. Clin Exp Pharmacol Physiol. 2008; 35(12):1405–1412. [PubMed: 18983577]
55. Leong CL, O'Connor PM, Eppel GA, Anderson WP, Evans RG. Measurement of renal tissue oxygen tension: systematic differences between fluorescence optode and microelectrode recordings in anaesthetized rabbits. Nephron Physiol. 2008; 108(2):p11–p17. [PubMed: 18223307]
56. Bonventre JV. Pathophysiology of AKI: injury and normal and abnormal repair. Contrib Nephrol. 2010; 165:9–17. [PubMed: 20427950]
57. Elias RM, Correa-Costa M, Barreto CR, Silva RC, Hayashida CY, Castoldi A, Goncalves GM, Braga TT, Barboza R, Rios FJ, Keller AC, Cenedeze MA, Hyane MI, D'Imperio-Lima MR, Figueiredo-Neto AM, Reis MA, Marinho CR, Pacheco-Silva A, Camara NO. Oxidative stress and modification of renal vascular permeability are associated with acute kidney injury during P. berghei ANKA infection. PLoS One. 2012; 7(8):e44004. [PubMed: 22952850]
58. Jordan BF, Cron GO, Gallez B. Rapid monitoring of oxygenation by 19F magnetic resonance imaging: Simultaneous comparison with fluorescence quenching. Magn Reson Med. 2009; 61(3): 634–638. [PubMed: 19097235]
59. Hunjan S, Zhao D, Constantinescu A, Hahn EW, Antich PP, Mason RP. Tumor oximetry: demonstration of an enhanced dynamic mapping procedure using fluorine-19 echo planar magnetic resonance imaging in the Dunning prostate R3327-AT1 rat tumor. Int J Radiat Oncol Biol Phys. 2001; 49(4):1097–1108. [PubMed: 11240252]
60. Hu L, Chen J, Yang X, Caruthers SD, Lanza GM, Wickline SA. Rapid quantification of oxygen tension in blood flow with a fluorine nanoparticle reporter and a novel blood flow-enhanced-saturation-recovery sequence. Magn Reson Med. 2012
61. Keupp J, Rahmer J, Grasslin I, Mazurkewitz PC, Schaeffter T, Lanza GM, Wickline SA, Caruthers SD. Simultaneous dual-nuclei imaging for motion corrected detection and quantification of 19F imaging agents. Magn Reson Med. 2011; 66(4):1116–1122. [PubMed: 21394779]
62. Messina EJ, Sun D, Koller A, Wolin MS, Kaley G. Increases in oxygen tension evoke arteriolar constriction by inhibiting endothelial prostaglandin synthesis. Microvasc Res. 1994; 48(2):151–160. [PubMed: 7854203]

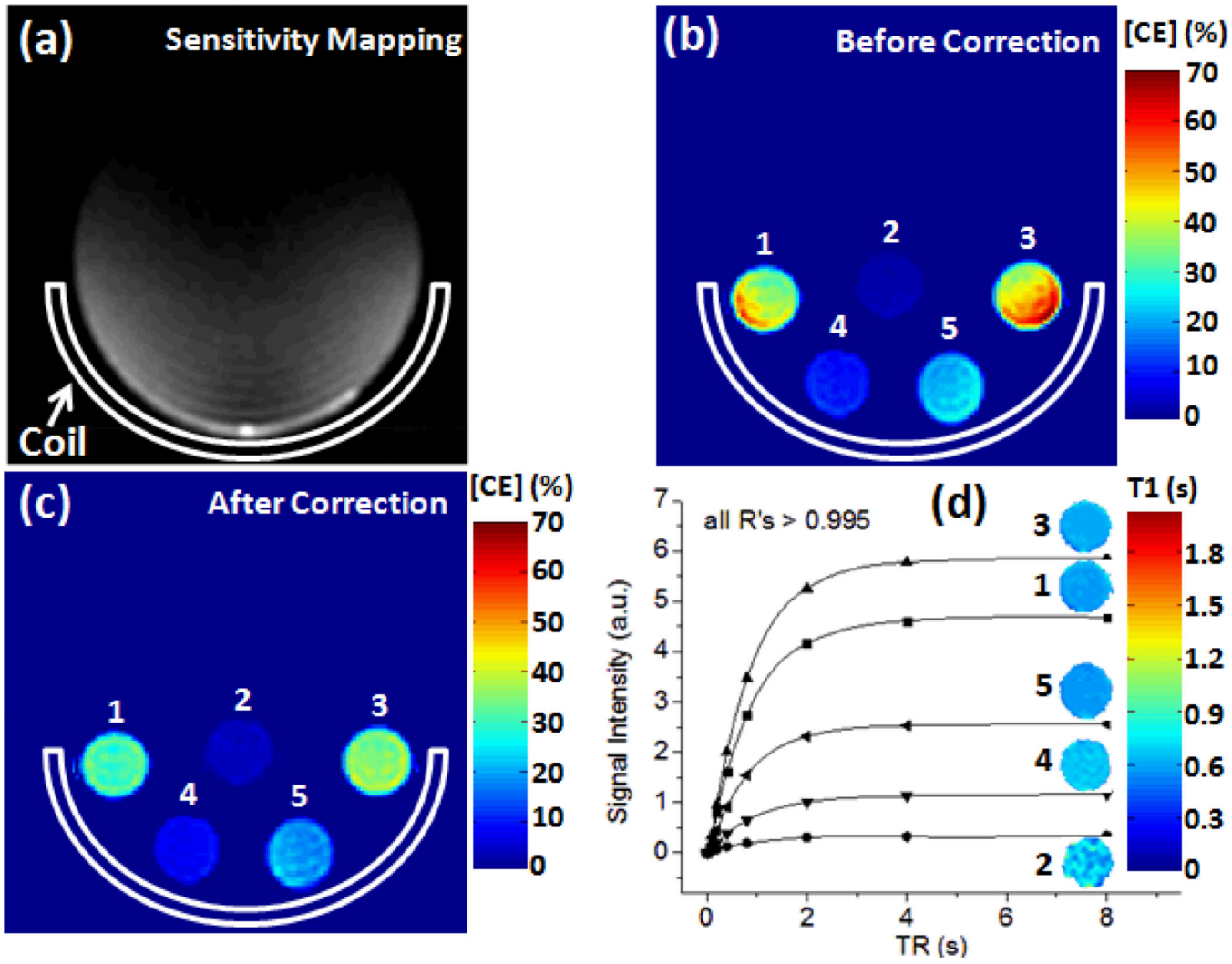

Figure 1.

(a) Sensitivity mapping of surface receive coil shows inhomogeous B1 map in a homogeneous phantom. (b & c) quantified CE concentration using 19F spin density weidghted MRI before and after coil sensitivity correction. (d) T1-weighted 19F signal recovery as a function of TR for different PFC NP phantoms. The inserted color images show the corresponding fitted T1 maps.

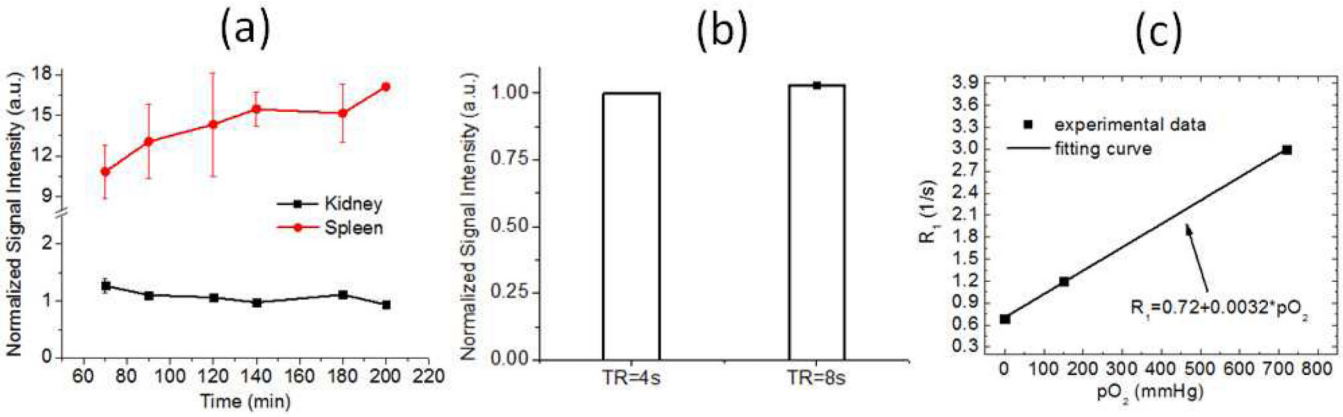

Figure 2.

(a) In vivo 19F MR spin density signal intensity in kidney and spleen shows the phamacokinetics of intraveneously injected CE NPs in normal mice (n=2). (b) In vivo fast spin-echo MRI detected comparable 19F signal intensity in mouse kidney for TR = 4s and 8s (n =2). (c) In vitro calibration shows 19F R1 of PFC Nps as a function of pO2. Data were collected at 11.7 T using a PFC NPs phantom with temperature maintained at 37°C. The correlation coefficient R > 0.09.

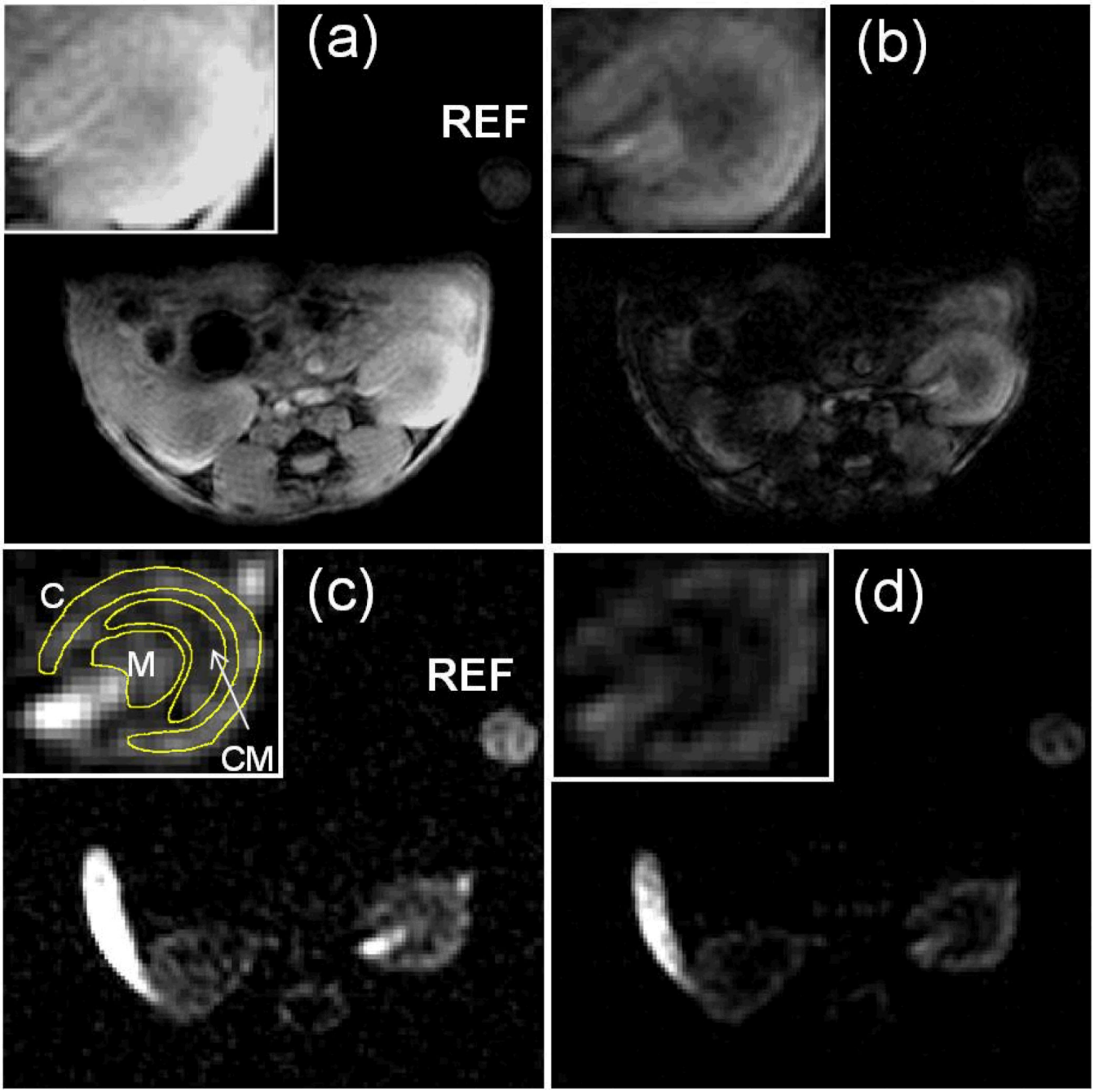

Figure 3.

(a & b) Representative T1-weighted and T2*-weighted ^{1}H MRI of mouse kidneys in the transverse plane. (c & d) Representative spin density weighted and T1-weighted ^{19}F MRI of mouse kidneys in the transverse plane. Slice planning is identical for ^{1}H and ^{19}F images and kidneys were zoomed in for better visualization. (C: cortex, CM: CM junction, M: medulla, REF: external reference standard).

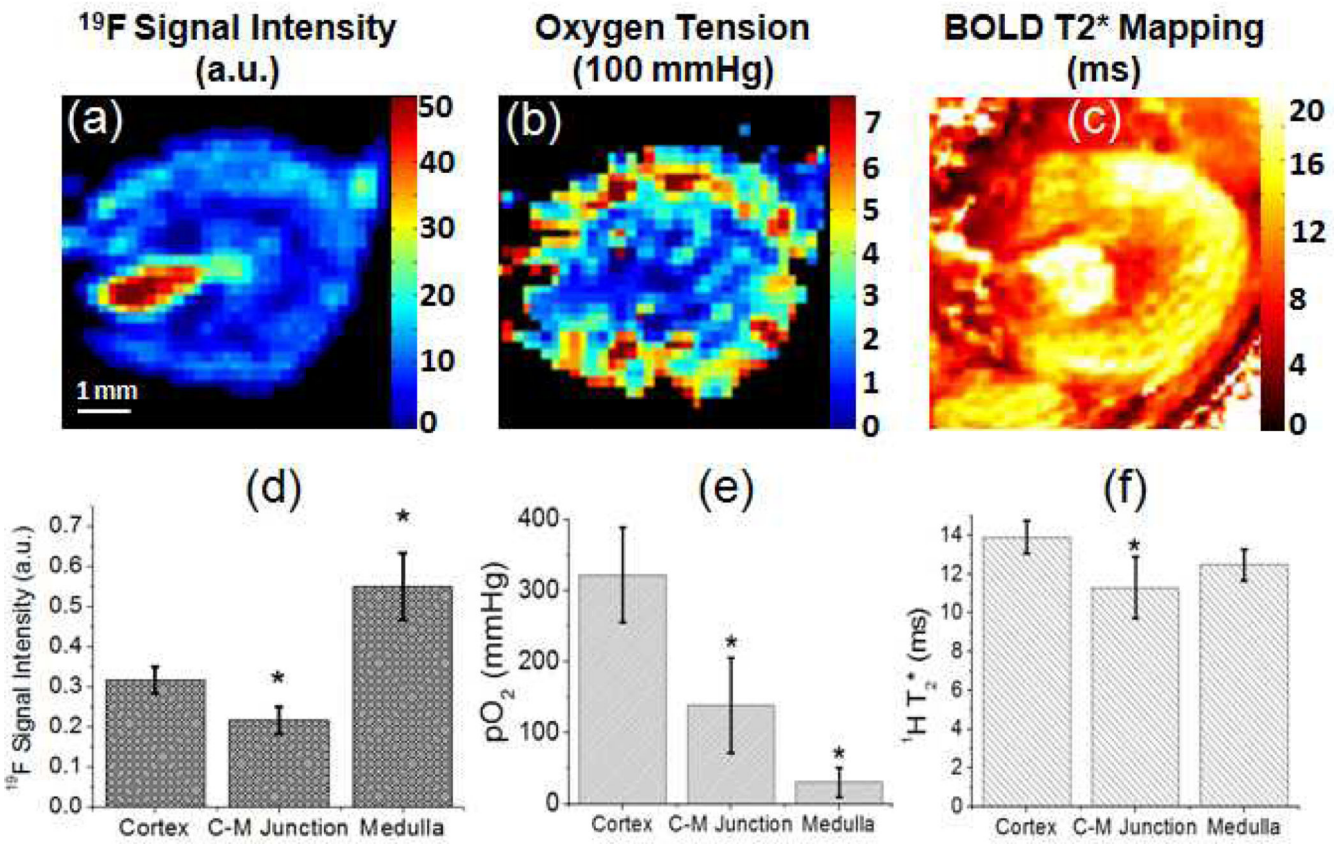

Figure 4.

(a–b) Representative quantitative renal blood volume and oxygen tension mapping generated from ^{19}F MRI of healthy kidneys. (c) Representative ^{1}H T2* mapping of healthy kidneys. (d–e) Quantification of functional indexes in different anatomical regions. Data were presented as mean ± std. (C–M: CM, *: $p<0.05$).

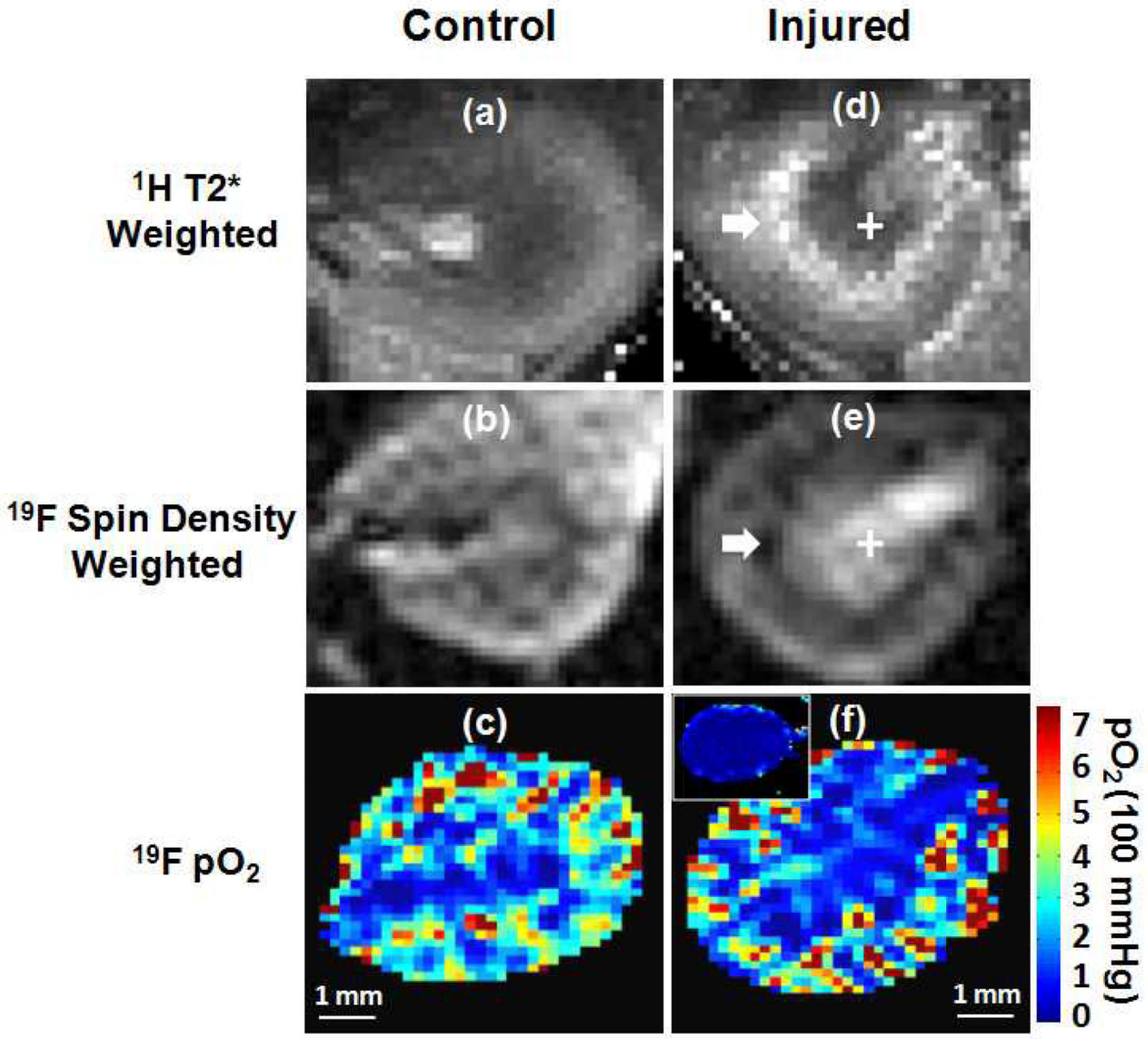

Figure 5.

Representative ^{1}H T2*-weighted image, ^{19}F spin density weighted image and pO2 mapping in contralateral and injured kidneys. The inserted panel in (f) represents the ^{19}F oxygenation mapping during ischemia. White arrow points to the CM junction and white cross identifies the renal medulla.

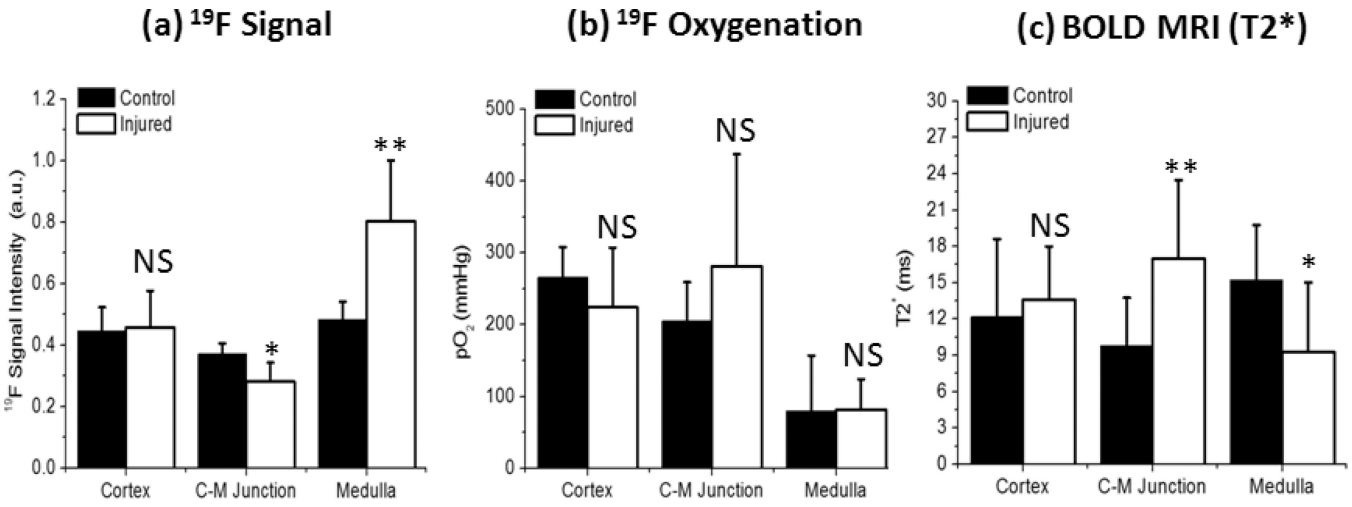

Figure 6.

Absolute quantification of ^{19}F signal intensity (a), pO2 (b) and ^{1}H T2* (c) in different anatomical regions of both contralateral and injured kidneys at 24 hours after injury. Data were presented as mean ± std. (*: $p<0.05$ and **: $p<0.01$).

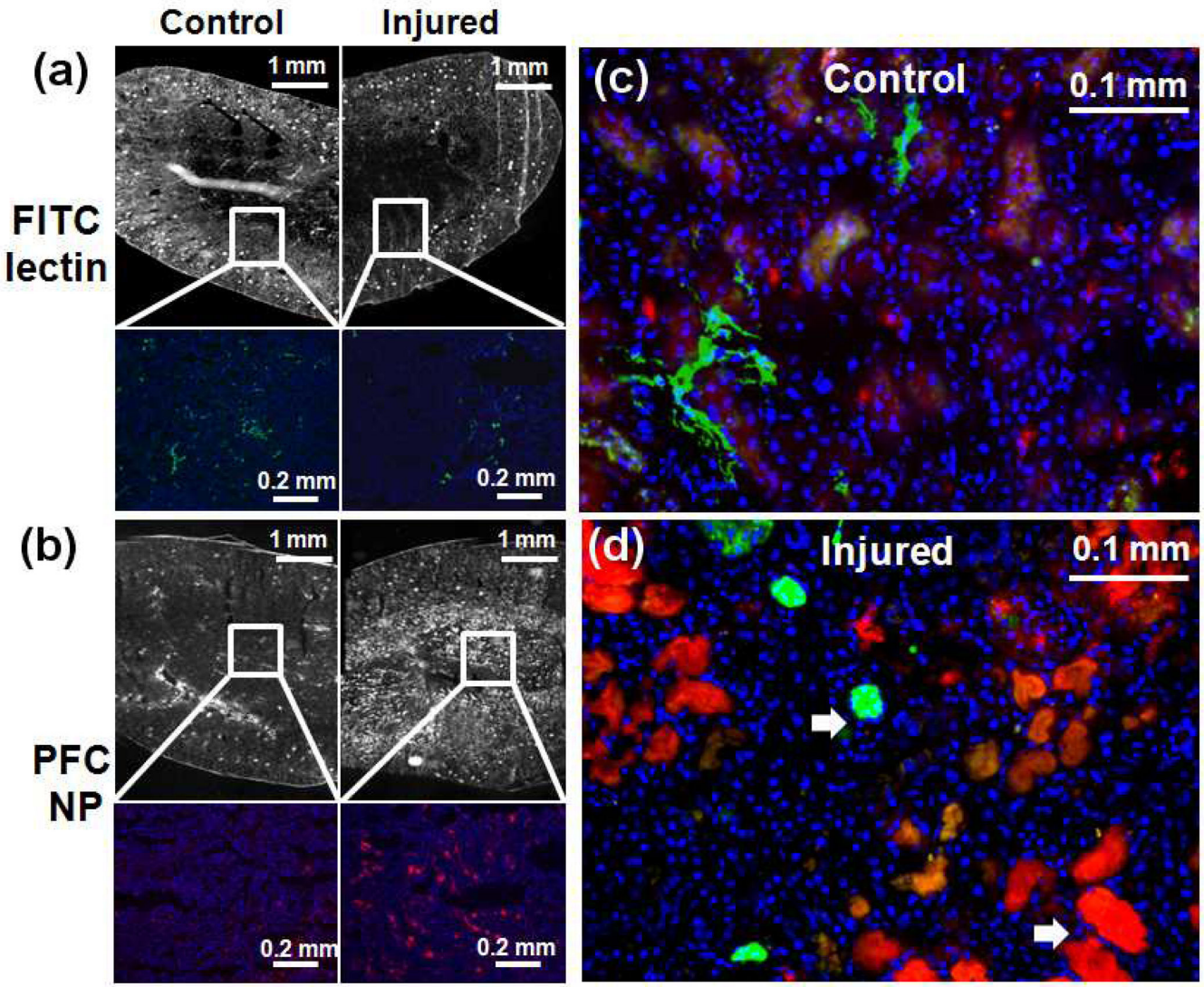

Figure 7.

(a) Top row: overview fluorescence image of FITC-lectin for visualizing perfused blood vessels in contralateral and injured kidneys. Bottom row: zoomed-in view of FITC-lectin fluorescence image in the CM junction. (b) Top row: overview fluorescence image of PFC NP in contralateral and injured kidneys. Bottom row: zoomed-in view of PFC NP fluorescence image in the renal medulla. (c & d) Merged FITC-lectin and PFC NP fluorescence image of renal medulla confirmed that PFC NP leaked out from blood vessels and accumulated in the extravascular space of injured kidneys as pointed by white arrows. (Red: PFC NP, Blue: DAPI, Green: FITC-lectin).

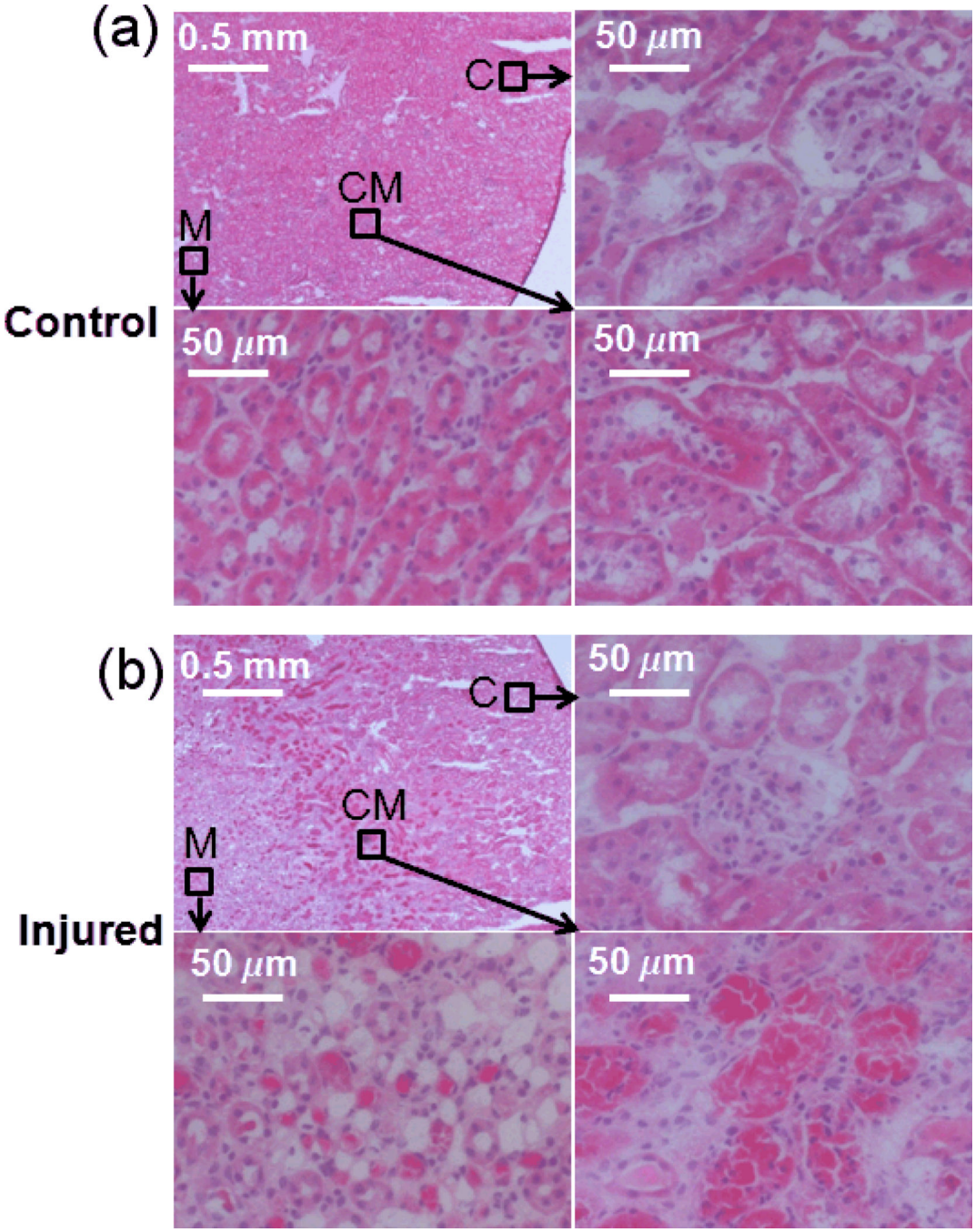

Figure 8.

(a & b) H&E staining of contralateral and injured kidneys. In both sub-figures, the top left panel is an overview of the kidney tissue and the other three panels are the high resolution pictures in different anatomical regions as indicated by dark arrows. H&E staining revealed extensive tissue damage and necrosis in the CM junction and in the medulla (C: cortex, CM: CM junction, M: medulla).